Research Article

Nano Research
2023, 16(4): 4656–4663

ISSN 1998-0124 CN 11-5974/O4
https://doi.org/10.1007/s12274-022-5112-x

Carbonitride MXene $Ti_3CN(OH)_x$@MoS_2 hybrids as efficient electrocatalyst for enhanced hydrogen evolution

Jizhou Jiang[1], Fangyi Li[1], Saishuai Bai[1], Yongjing Wang[1], Kun Xiang[1] (✉), Haitao Wang[1], Jing Zou[1], and Jyh-Ping Hsu[2] (✉)

[1] *School of Environmental Ecology and Biological Engineering, School of Chemistry and Environmental Engineering, Key Laboratory of Green Chemical Engineering Process of Ministry of Education, Engineering Research Center of Phosphorus Resources Development and Utilization of Ministry of Education, Novel Catalytic Materials of Hubei Engineering Research Center, Wuhan Institute of Technology, Wuhan 430205, China*

[2] *Department of Chemical Engineering, "National Taiwan University", Taipei 10617*

Received: 10 July 2022 / **Revised:** 28 September 2022 / **Accepted:** 28 September 2022

ABSTRACT

Renewable energy powered electrocatalytic water splitting is a promising strategy for hydrogen generation, and the design and development of high-efficiency and earth-abundant electrocatalysts for hydrogen evolution reaction (HER) are highly desirable. Herein, MoS_2 nanoflowers decorated two-dimensional carbonitride-based MXene $Ti_3CN(OH)_x$ hybrids have been constructed by etching and post-hydrothermal methods. The electrochemical performance of the as-obtained $Ti_3CN(OH)_x$@MoS_2 hybrids having a quasi core–shell structure is fascinating: An overpotential of 120 mV and a Tafel slope of 64 mV·dec^{-1} can be delivered at a current density of 10 mA·cm^{-2}. And after 3,000 cyclic voltammetry cycles, it can be seen that there is no apparent attenuation. Both the experimental results and density functional theory (DFT) calculations indicate that the synergetic effects between $Ti_3CN(OH)_x$ and MoS_2 are responsible for the robust electrochemical HER performance. The electrons of –OH group in $Ti_3CN(OH)_x$ are transferred to MoS_2, making the adsorption energy of the composite for H almost vanish. The metallic $Ti_3CN(OH)_x$ is also beneficial to the fast charge transfer kinetics. The construction of MXene-based hybrids with optimal electronic structure and unique morphology tailored to the applications can be further used in other promising energy storage and conversion devices.

KEYWORDS

$Ti_3CN(OH)_x$, MoS_2, hydrogen evolution reaction, density functional theory (DFT) calculations

1 Introduction

Being a clean secondary energy carrier, hydrogen has the characteristics of, for example, high energy density (3, 3.9, and 4.5 times of gasoline, alcohol, and coke, respectively) and zero carbon emission (only water). It is widely used in hydrogen fuel cells and a variety of green chemical processes, and is becoming the "future star" of global clean energy [1–3]. Being a facile and environmental-friendly process [4], the hydrogen evolution reaction (HER) through electrolytic water splitting by renewable energy is in the ascendant. However, due to the sluggish kinetic process of HER, the electrocatalytic reaction has a high overpotential, resulting in inadequate energy efficiency for HER [5], and only 3.9% of the world's hydrogen demand is satisfied by electrolysis. Hence, it is imperative to seek a system for efficient electrocatalytic HER. During these HER systems, the design and construction of the catalyst is one of the most critical factors.

To date, Pt-based materials are widely regarded as the most suitable and efficient electrocatalysts for HER [1, 4]. Their high cost and poor durability, however, suggest that developing non-noble metal-based electrocatalysts having excellent electrochemical performance is necessary [6–10]. Among numerous candidates, two-dimensional (2D) transition metal carbides, nitrides, and carbonitrides (MXene) have attracted the attention of researchers considering their good electrical conductivity, high carrier mobility, fascinating structure, and excellent hydrophilicity [11–15]. Generally, the chemical formula of MXene is $M_{n+1}X_nT_x$, where M, X, and T represent an early transition metal, carbon or/and nitrogen, and surface termination, respectively [16, 17]. What's more, the selective etching of the A layer off the MAX phase [18] yields abundant surface functional terminations such as –Cl, –F, –OH, and –O–. Specifically, theoretical calculations and experimental observations all suggest that the –OH terminations on the basal planes of MXene exhibit considerable HER properties [19]. However, due to the oxophilic feature of metal in air and/or water [20], MXenes are easily transferred to metal oxides. Therefore, the electrochemical performance of hybridizing MXene with active armor can be further improved by modulating the Gibbs free energy for hydrogen adsorption (ΔG_H^*) [21, 22]. It was reported recently that the electrocatalytic HER performance of composites can be significantly improved by combining metal nanoparticles [23], transition metal nitrides [24], chalcogenides [25, 26], phosphide [27, 28], carbide [29], hydroxides [30], and oxides [31, 32] on the surface of MXenes to form hybrids. Especially, due to its unique structure properties and instinct activity toward HER in diverse pH, MoS_2 has been widely

Address correspondence to Kun Xiang, xiangkun@wit.edu.cn; Jyh-Ping Hsu, jphsu@ntu.edu.tw

investigated as a newly developed 2D material. For example, Liu et al. fabricated a $MoS_2/Ti_3C_2T_x$ heterostructure on Ni foam for HER [33], where the overpotential is 209 mV at 10 mA·cm^{-2} in a 1 M KOH, lower than that of $Ti_3C_2T_x$ or MoS_2 electrode. If 0.5 M H_2SO_4 is used as the acidic electrolyte, the optimized ultrafine $Ti_3C_2T_x$ MXene nanosheets electrode, decorated by MoS_2 quantum dot (QD), requires only ca. 280 mV overpotential to reach a benchmark HER at 10 mA·cm^{-2}, notably superior to both pristine MoS_2 QDs and $Ti_3C_2T_x$ electrodes. The synergetic coupling effects and remarkable structural features of MoS_2 QDs-$Ti_3C_2T_x$ are responsible for the promising HER activity [34]. Although some progress has been made, hybridizing OH-terminated carbonitride-based MXene with MoS_2 to boost HER performance is still more challenging.

In this work, quasi core–shell structural carbonitride-based MXene $Ti_3CN(OH)_x$@MoS_2 hybrids are prepared by *in situ* etching coupled with post hydrothermal synthesis. Benefiting from fast charge transfer kinetics, regulated electronic structure, strong interactions, and synergistic effect between them, the as-obtained quasi core–shell structural $Ti_3CN(OH)_x$@MoS_2 hybrids exhibit an optimal ΔG_H*, which boosts HER activity with a low overpotential of 120 mV at a current density of 10 mA·cm^{-2} in 0.5 M H_2SO_4. Furthermore, the electrochemical activity of the quasi core–shell structural $Ti_3CN(OH)_x$@MoS_2 is essentially unchanged after 3,000 cyclic voltammetry (CV) cycles, suggesting the excellent long-term durability. Moreover, the electronic microstructure and enhanced HER mechanism of the quasi core–shell structural $Ti_3CN(OH)_x$@MoS_2 hybrids have been also investigated by density functional theory (DFT) calculations, including the charge density difference (CDD) spectra, the electron localization function (ELF) mapping, and the density of states (DOS) analysis. These describe vividly the transfer of interface charges from $Ti_3CN(OH)_x$ nanosheets to MoS_2 nanoflowers, and the presence of an asymmetric electronic localization deflection of surface/interface atoms. We verified vigorously from both experimental and theoretical aspects that the MXene-based hybrids can be employed as highly efficient HER catalysts.

2 Experimental section

2.1 Synthesis of $Ti_3CN(OH)_x$

20 mL of 9 M HCl was first prepared and placed in a teflon bottle. 1.6 g of LiF was then weighed and dissolved inside. After the two reagents were evenly mixed, 1 g of Ti_3AlCN was introduced, and the aluminum layer in Ti_3AlCN was removed by etching for 48 h. The suspension obtained was centrifuged at 3,500 rpm for 1 min, and 2 M HCl was then introduced to wash off unreacted LiF. Adding deionized water, centrifugation, and washing were repeated until the pH of the supernatant reached 7. After ultrasonic exfoliation for 30 min, the precipitate was vacuum-dried at 60 °C to obtain Ti_3CNT_x. The as-obtained powder was placed in an excess of 10 wt.% KOH solution, and stirred at 25 °C for 4 h to replace the –F end group with –OH groups. The resulting suspension was placed in a centrifuge tube and centrifuged at 3,500 rpm. Ultrapure water was introduced for washing and centrifuged 5 times until the pH of the supernatant was 7. It was then dried to obtain $Ti_3CN(OH)_x$ powder.

2.2 Synthesis of $Ti_3CN(OH)_x$@MoS_2

0.8 g of thiourea and 0.5 g of ammonium molybdate tetrahydrate were first dissolved in 60 mL of deionized water, followed by slowly introducing a certain amount of $Ti_3CN(OH)_x$-MXene. The resulting solution was sonicated to make it homogeneous, which was then transferred to a 100 mL high-pressure reaction kettle. The reaction was conducted at 180 °C for 12 h, and after cooled to 25 °C, the product was filtered and rinsed with deionized water three times. Finally, the sample was vacuum dried at 60 °C. The influences of sulfur source, hydrothermal time, temperature, and type of terminal functional groups were studied.

2.3 Electrochemical measurements

4 mg of catalyst was dispersed in 1 mL of 0.1% Nafion solution and sonicated for 60 min to form a homogeneous solution. Then, 20 μL of the solution obtained was dripped onto a clean glassy carbon electrode (Φ = 5 mm), which was the working electrode after drying. The mass loading was about 0.408 mg·cm^{-2}. All the electrochemical measurements were made in 0.5 M H_2SO_4 by a three-electrode system using CHI 760E electrochemical workstation. Ag/AgCl and graphite rod served as reference electrode and counter electrode, respectively. The linear sweep voltammetry (LSV) curves of as-prepared samples were recorded at a scan rate of 5 mV·s^{-1}. The double-layer capacitance (C_{dl}) was evaluated by CV at a scan rate ranging from 10 to 120 mV·s^{-1} at a potential ranging from 0.4 to 0.5 V vs. reversible hydrogen electrode (RHE). Electrochemical impedance spectroscopy (EIS) was measured at a frequency ranging from 10 to 1 MHz with 5 mV amplitude to estimate the interface charge transfer. The stability of the catalyst was evaluated by a continuous CV cycle and chronoamperometry method. The potentials in all measurements were converted to standard RHE by Eq. (1), 90% *iR* compensation was made for all electrochemical measurements

$$E_{RHE} = E_{Ag/AgCl} + 0.059 \times pH + E \quad (1)$$

2.4 Theoretical calculations

The DFT calculations were conducted by Vienna *ab initio* package (VASP). Structural optimization, electronic structure, and ΔG_H* regarding MoS_2, $Ti_3CN(OH)_x$, and $Ti_3CN(OH)_x$@MoS_2 hybrids were all investigated via DFT calculations. The details are described in the Electronic Supplementary Material (ESM).

3 Results and discussion

In brief, free-standing Ti_3CNT_x nanosheets are obtained by selective etching of Al in Ti_3AlC_2 phase in LiF and HCl mixed solution and post exfoliation treatment by bath sonicated for 48 h. Then, $Ti_3CN(OH)_x$ nanosheets are formed by alkaline treatment in 10 wt.% KOH. Finally, flower-like MoS_2 uniformly grows on the $Ti_3CN(OH)_x$ surface through the hydrothermal method (Fig. 1).

Both the morphology and the elemental distribution of $Ti_3CN(OH)_x$@MoS_2 hybrids are characterized by scanning electron microscopy (SEM). As shown in Fig. 2(a), pristine MoS_2 displays unique flower-like structure having a diameter of about 150 nm. Typically, the nanoflower-like structure has abundant folds and appropriate cavities, making pristine MoS_2 conducive in an electrolyte solution thereby improving its electrocatalytic performance. Figure 2(b) shows representative free-standing $Ti_3CN(OH)_x$ nanosheets. It is clear that sonication can well exfoliate the bulk MXene materials into nanosheet-like structures. In general, the 2D metallic MXene can significantly facilitate the charge transfer during electrocatalytic reactions. Figure 2(c) illustrates an SEM image of $Ti_3CN(OH)_x$@MoS_2 hybrids. As seen, MoS_2 nanoflowers are homogeneously and tightly attached to $Ti_3CN(OH)_x$ nanosheet to form quasi core–shell structure of $Ti_3CN(OH)_x$@MoS_2 hybrids. The element mapping images of $Ti_3CN(OH)_x$@MoS_2 hybrids suggest that Ti, C, N, O, Mo, and S elements are co-existence and homogeneously distributed over its entire structure (Fig. 2(d)). The morphology and structure of

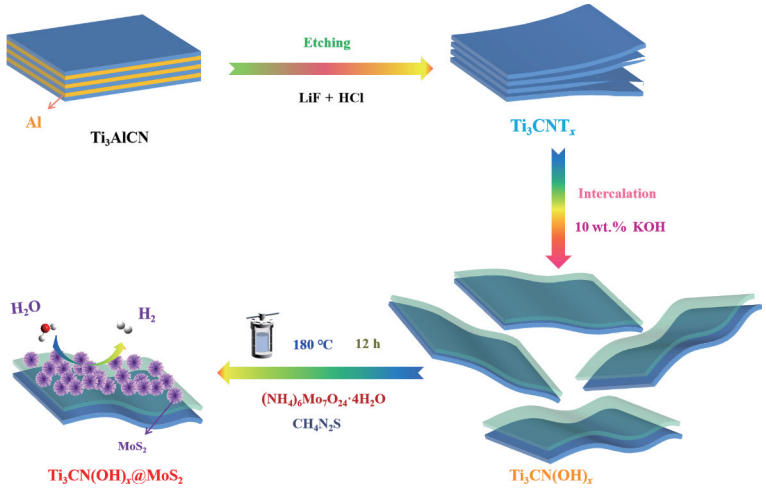

Figure 1 Schematic illustration of the fabrication procedure of $Ti_3CN(OH)_x@MoS_2$ hybrids.

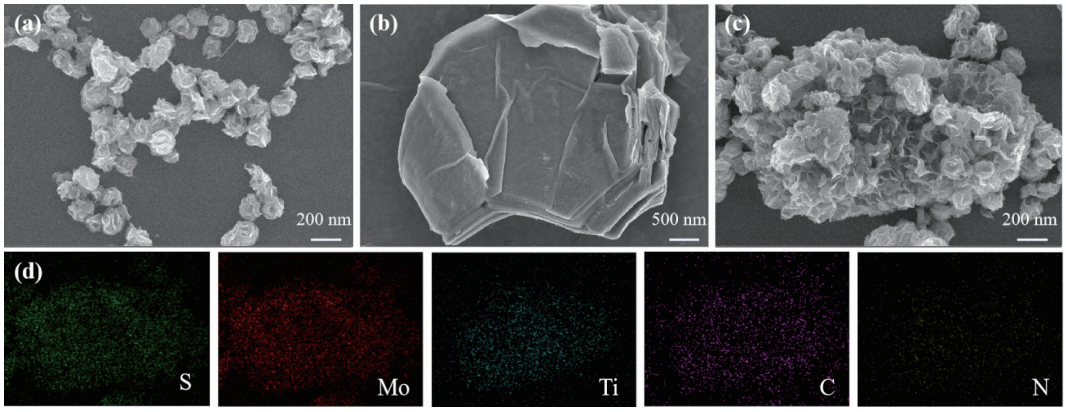

Figure 2 SEM images of (a) MoS_2 nanoflowers, (b) $Ti_3CN(OH)_x$ nanosheets, and (c) $Ti_3CN(OH)_x@MoS_2$ hybrids. (d) Elemental mapping corresponding to (c).

$Ti_3CN(OH)_x@MoS_2$ hybrids are further characterized by high-resolution transmission electron microscopy (HRTEM). Figure S1 in the ESM illustrates the typical 2D nanosheets and the layers of MoS_2 stacking together along the *c*-axis.

The transformation of Ti_3AlCN to Ti_3CNT_x MXene can be confirmed by X-ray diffraction (XRD) (Fig. 3(a)), where the disappearance of the (104) diffraction peak of Ti_3AlCN MAX at 2θ = 39° is attributed to the etch of the Al layer [35, 36]. The peak of $Ti_3CN(OH)_x$ at 2θ = 6° reveals that the layer spacing of MXene increases significantly [37, 38]. The XRD patterns show no changes in the crystal structure of Ti_3CNT_x and $Ti_3CN(OH)_x$, indicating that their structures are not affected by different terminal groups (–F and –OH). Moreover, there are still two less prominent diffraction peaks at 32°–27° and 57.4°, corresponding to the (100) + (101) and (110) crystal planes of MoS_2, respectively. These diffraction peaks are broad and weak, indicating that MoS_2 has a poor crystallinity rather than an amorphous structure [39, 40]. However, in the case of constructive interference from the aligned crystal planes, the relevant diffraction peak at 14.4° disappears, indicating a significantly reduced aggregation of the resulting MoS_2 nanosheets along the *c*-axis. The Raman spectra of $Ti_3CN(OH)_x$, MoS_2, and $Ti_3CN(OH)_x@MoS_2$ were also recorded (Fig. S2 in the ESM). The $Ti_3CN(OH)_x$ MXene signals appear at 402, 512, and 628 cm^{-1}. The Raman spectrum of MoS_2 displays these characteristic peaks related to J_2 and J_3 longitudinal acoustic phonon modes around 237 and 337 cm^{-1}, confirming the 1T phase of MoS_2. A small peak at 377 cm^{-1} corresponding to the E_{2g}^1 of the 2H-phase of MoS_2 indicates that MoS_2 mainly exists in the form of 1T-MoS_2. Furthermore, the presence of the E_{1g} Raman peaks at 282 cm^{-1} suggests the octahedral coordination of Mo in 1T-MoS_2 [41, 42]. Interestingly, distinct characteristic signals of MoS_2 and weak signals of $Ti_3CN(OH)_x$ can be seen in the hybrids, indicating the formation of quasi core–shell $Ti_3CN(OH)_x@MoS_2$ hybrids. The TEM images and Raman spectra of the nanocomposite verify the structure of the unique quasi core–shell $Ti_3CN(OH)_x@MoS_2$ hybrids.

Both the surface chemical composition and the chemical states of as-obtained materials are illuminated through X-ray photoelectron spectroscopy (XPS) analysis. The Mo 3d fine-scan spectra of MoS_2 and $Ti_3CN(OH)_x@MoS_2$ hybrids (Fig. 3(c)) have two main peaks at 228.3 and 231.6 eV, which are assigned to the Mo $3d_{5/2}$ and Mo $3d_{3/2}$ of Mo–S bonds, respectively. It is worth noting that the binding energies of the Mo $3d_{5/2}$ and Mo $3d_{3/2}$ peaks of $Ti_3CN(OH)_x@MoS_2$ hybrids shifted negatively compared to those of pristine MoS_2, convincingly suggesting the strong electronic interaction between MoS_2 and $Ti_3CN(OH)_x$ nanosheets. The other peaks with binding energies at 229.1 and 232.8 eV correspond to Mo $3d_{5/2}$ and Mo $3d_{3/2}$ of Mo–O bonds, respectively. The higher spin-orbit splitting doublets with peaks of 235.4 and 235.9 eV are related to the Mo^{6+} species [42, 43]. In addition, the characteristic peak located at 225.6 eV belongs to S 2s [44]. The binding energies at 161.4 and 162.4 eV (Fig. 3(d)) are attributed to the S $2p_{3/2}$ and $2p_{1/2}$ orbitals of S^{2-}, respectively, and the peaks at 163.0 and 164.1 eV to the presence of bridging S_2^{2-} or apical S_2^{2-} resulting from the unsaturated S atoms in low crystallinity MoS_2 [43]. The peaks with high binding energies of 168.1 and 169.2 eV for MoS_2 arise from unavoidable oxidation [45]. In the case of $Ti_3CN(OH)_x@MoS_2$ hybrids, the new C–S–C peaks at 163.1 and 164.0 eV appeared except for the S 2p peaks, further illustrating the interaction between MoS_2 and $Ti_3CN(OH)_x$ nanosheets [42, 46]. Intuitively, this indicates the transfer of electrons from $Ti_3CN(OH)_x$ to MoS_2 at the $Ti_3CN(OH)_x@MoS_2$

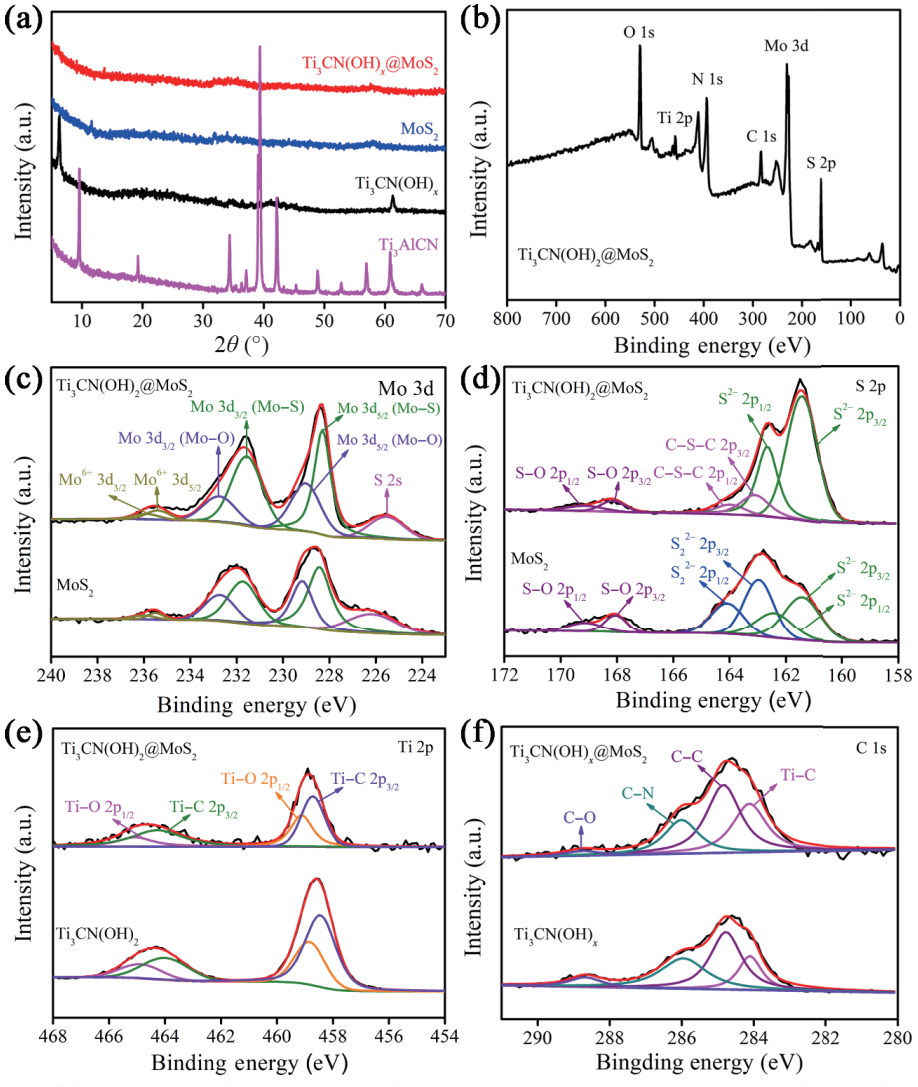

Figure 3 (a) XRD patterns of the MAX phase of Ti_3AlCN, Ti_3CNCl_2, $Ti_3CN(OH)_x$, MoS_2, and $Ti_3CN(OH)_x$@MoS_2 hybrids. (b) Survey XPS spectrum of $Ti_3CN(OH)_x$@MoS_2 hybrids. High-resolution spectra of (c) Mo 3d, (d) S 2p, (e) Ti 2p, and (f) C 1s, before and after hybridization.

hybrids interface. The Ti 2p spectra demonstrated in Fig. 3(e) have four primary peaks at 458.7, 459.1, 464.2, and 465.0 eV, corresponding to Ti–C $2p_{3/2}$, Ti–O $2p_{1/2}$, Ti–C $2p_{3/2}$, and Ti–O $2p_{1/2}$ bonds, respectively. Due to the transfer of electrons from $Ti_3CN(OH)_x$ to MoS_2, the binding energy of Ti 2p peaks of $Ti_3CN(OH)_x$@MoS_2 hybrids shifted to a higher value compared to the case of $Ti_3CN(OH)_x$ [36, 38]. These characterization results of $Ti_3CN(OH)_x$@MoS_2 hybrids fully illustrate the formation of a quasi core–shell structure and the interaction between them.

The CDD is also investigated to explore the charge transfer and distribution at the interface of $Ti_3CN(OH)_x$ nanosheets and MoS_2 nanoflowers. The yellow regions around S atoms in Fig. 4(a) and Fig. S3 in the ESM indicate charge accumulation, and the blue regions near O atoms indicate charge depletion. These suggest that the electrons of the O of $Ti_3CN(OH)_x$ nanosheets transferred to the S of MoS_2 nanoflowers through the interface of quasi core–shell structural $Ti_3CN(OH)_x$@MoS_2 hybrids. To investigate the degree of electron localization, we plot the ELF pattern of quasi

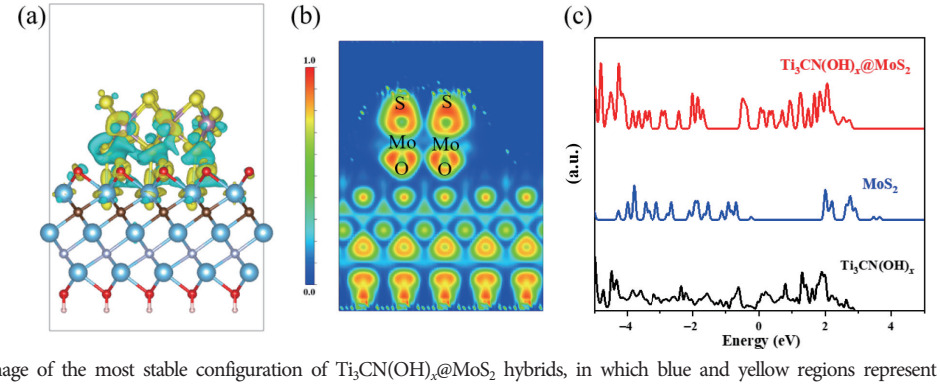

Figure 4 (a) CDD image of the most stable configuration of $Ti_3CN(OH)_x$@MoS_2 hybrids, in which blue and yellow regions represent electron depletion and accumulation, respectively. (b) ELF pattern of $Ti_3CN(OH)_x$@MoS_2 hybrids. (c) DOS curves for $Ti_3CN(OH)_x$ nanosheets, MoS_2 nanoflowers, and $Ti_3CN(OH)_x$@MoS_2 hybrids, respectively.

core–shell structural $Ti_3CN(OH)_x$@MoS_2 hybrids in Fig. 4(b). As seen, the electron distributions of S and O at the interface are asymmetric, suggesting the presence of chemical bonding between $Ti_3CN(OH)_x$ nanosheets and MoS_2 nanoflowers at the interface. Compared with the vacuum layer, the O atom around the interface has a lower degree of electron localization, and also verifies the transfer of the electron of O to S. Furthermore, the interaction between $Ti_3CN(OH)_x$ nanosheets and MoS_2 nanoflowers is studied by calculating the DOS of $Ti_3CN(OH)_x$, MoS_2, and $Ti_3CN(OH)_x$@MoS_2 hybrids. As shown in Fig. 4(c), several peaks are present in the DOS plots of $Ti_3CN(OH)_x$ and MoS_2, indicating their electrons are localized. In contrast, the DOS plot of $Ti_3CN(OH)_xMoS_2$ hybrids is evenly distributed after hybridization for the energy range examined, indicating that electrons are more favorable to interact with H^+. The experimental and theoretical results presented above verify the presence of chemical interaction between the –OH group on the surfaces of $Ti_3CN(OH)_x$ and the MoS_2 at the interface. The non-simple physical combination of the quasi core–shell structural $Ti_3CN(OH)_x$@MoS_2 hybrids with modulated electronic structure raises its stability and makes it have an excellent charge transfer kinetics, which is beneficial to boost HER activity [47].

The electrochemical performance of the electrocatalysts prepared was evaluated by a three-electrode configuration in a 0.5 M H_2SO_4. The potentials mentioned in this work are all corrected for ohmic potential drop with 90% *iR* compensation. In order to optimize the synthesis conditions, $Ti_3CN(OH)_x$@MoS_2 hybrids having different hydrothermal times are prepared, and their electrochemical performance is depicted in Figs. S4(a) and S4(b) in the ESM. Among the electrodes examined, the quasi core–shell structural $Ti_3CN(OH)_x$@MoS_2 hybrids resulting from 12 h hydrothermal time show the optimal HER activity, where the overpotential is 120 mV when the current density is 10 mA·cm^{-2}. The influence of hydrothermal temperature on electrode performance was also investigated. As shown in Figs. S4(c) and S4(d) in the ESM, the optimum temperature is 180 °C. Note that, a too short reaction time and a low temperature may induce insufficient coupling between $Ti_3CN(OH)_x$ and MoS_2, while a too long reaction time and a high temperature may result in serious agglomeration or restacking, lowering directly the HER activity of the quasi core–shell structural $Ti_3CN(OH)_x$@MoS_2 hybrids.

To illustrate the synergistic effect of the quasi core–shell structural $Ti_3CN(OH)_x$@MoS_2 hybrids in HER performance, pristine Ti_3CNT_x, $Ti_3CN(OH)_x$, and pure MoS_2 are used as references for comparison. LSV curves of Ti_3CNT_x, $Ti_3CN(OH)_x$, MoS_2, and $Ti_3CN(OH)_x$@MoS_2 hybrids are conducted at a scan rate of 5 mV·s^{-1}, and the results obtained are presented in Fig. 5(a). Specifically, the quasi core–shell structural $Ti_3CN(OH)_x$@MoS_2 hybrids electrode exhibits a satisfactory HER performance, where the overpotential is 120 mV at a current density of 10 mA·cm^{-2}, considerably lower than the corresponding values of Ti_3CNT_x (> 350 mV), $Ti_3CN(OH)_x$ (201 mV), and MoS_2 (248 mV). Furthermore, the ultralow potential is advantageous over most of the state-of-the-art Mo-based electrocatalysts (Table S1 in the

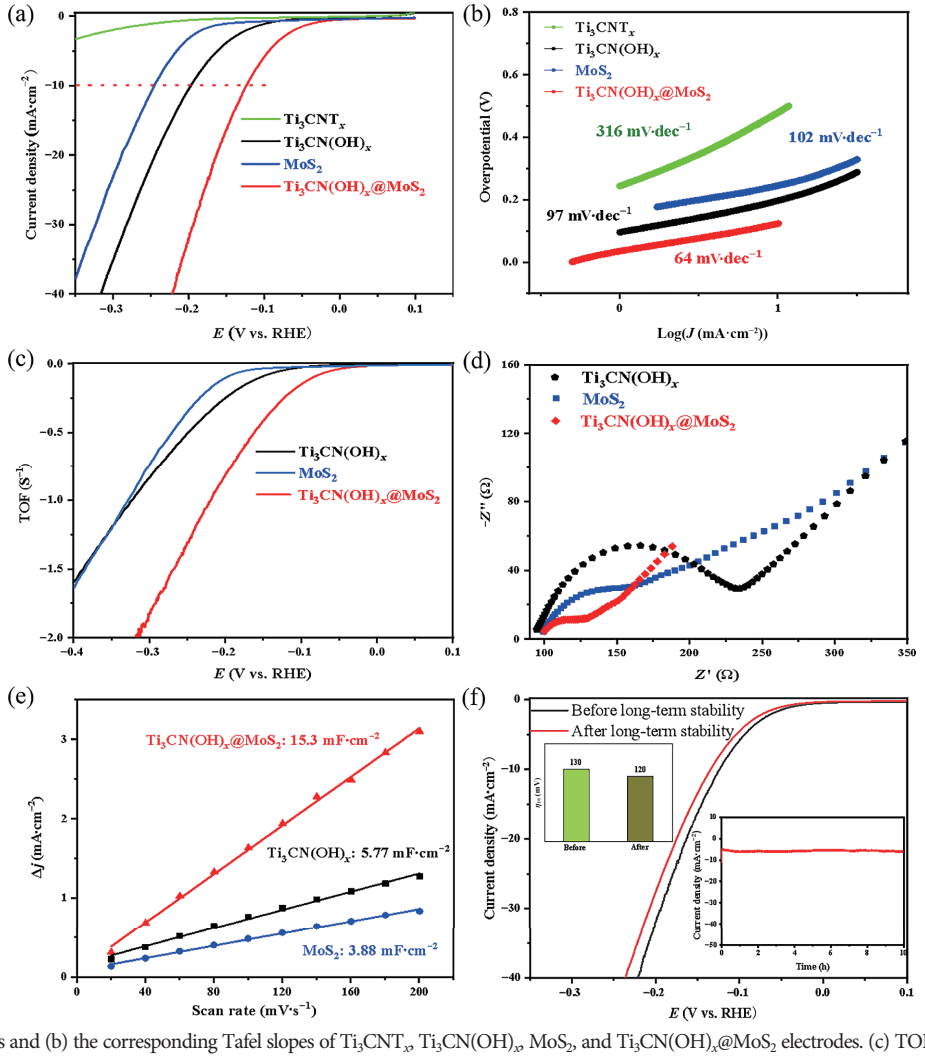

Figure 5 (a) LSV curves and (b) the corresponding Tafel slopes of Ti_3CNT_x, $Ti_3CN(OH)_x$, MoS_2, and $Ti_3CN(OH)_x$@MoS_2 electrodes. (c) TOF curves and (d) Nyquist plots of Ti_3CNCl_2, CoS_2, and Ti_3CNCl_2@CoS_2 modified electrodes. (e) The difference in current density ($\Delta j = 1/2(j_a - j_c)$) against scan rate of $Ti_3CN(OH)_x$, MoS_2, and $Ti_3CN(OH)_x$@MoS_2 modified electrodes. (f) LSV curves of Ti_3CNCl_2@CoS_2 modified electrode before and after long-term HER tests. Inset: long-term durability test.

ESM). To investigate the electrocatalytic kinetics of these as-obtained catalysts, the Tafel slopes are calculated, and the results are 64, 316, 97, and 102 mV·dec^{-1} for $Ti_3CN(OH)_x$@MoS_2 hybrids, Ti_3CNT_x, $Ti_3CN(OH)_x$, and pure MoS_2, respectively (Fig. 5(b)). The smallest Tafel slope of the quasi core–shell structural $Ti_3CN(OH)_x$@MoS_2 hybrids indicates that the coupling of $Ti_3CN(OH)_x$ and MoS_2 is kinetically beneficial for electrocatalytic HER. The relationship between the Tafel slope and HER suggests that Volmer–Heyrovsky is the rate-controlling step of the HER mechanism of the quasi core–shell structural $Ti_3CN(OH)_x$@MoS_2 hybrids.

Turnover frequency (TOF) is another key factor to measure the intrinsic electrochemical activity used to evaluate HER performance. Figure 5(c) shows the variation of TOF as a function of potential for the electrodes studied. The TOF values delivered by the quasi core–shell structural $Ti_3CN(OH)_x$@MoS_2 hybrids electrode are 0.21, 0.88, and 1.91 at potentials of 100, 200, and 300 mV, respectively. This is much higher than those of single $Ti_3CN(OH)_x$ and MoS_2 electrodes. In the range of voltage considered, the quasi core–shell structural $Ti_3CN(OH)_x$@MoS_2 hybrids electrode exhibits the largest TOF value, indicating that it has exceptional HER activity. To further explore the electrochemical kinetics process, we measured the EIS of $Ti_3CN(OH)_x$, MoS_2, and $Ti_3CN(OH)_x$@MoS_2 hybrids electrodes. As seen in Fig. 5(d), the resistance of charge transfer can be represented by the semicircles in the EIS curves. This confirms that the quasi core–shell structural $Ti_3CN(OH)_x$@MoS_2 hybrids electrode has the smallest charge transfer resistance compared to $Ti_3CN(OH)_x$ and MoS_2, suggesting the favorable HER kinetic process occurring at the electrode and electrolyte interface. Based on C_{dl}, we also evaluate the electrochemical active surface area of these electrocatalysts, and the results obtained are presented in Fig. 5(e) and Fig. S5 in the ESM. The estimated C_{dl} of the quasi core–shell structural $Ti_3CN(OH)_x$@MoS_2 hybrids is 15.3 mF·cm^{-2}, 2.65 and 3.94 times that of $Ti_3CN(OH)_x$ electrode and MoS_2 electrode, respectively. These reveal that the exposure of the available active sites for HER is high after the coupling between $Ti_3CN(OH)_x$ and MoS_2. Another important indicator for assessing the performance of electrocatalysts is their long-term stability. As can be seen in Fig. 5(f), the LSV curve of the quasi core–shell structural $Ti_3CN(OH)_x$@MoS_2 hybrids catalyst after 3,000 CV cycles is essentially the same as that initially. Chronoamperometry measurements for the quasi core–shell structural $Ti_3CN(OH)_x$@MoS_2 hybrids electrode are also carried out at a potential of −0.12 V (vs. RHE) and the steady HER current density is retained for 10 h. These measurements reveal the outstanding structural robustness in the electrocatalytic HER process. These results demonstrate that the unique quasi core–shell structural $Ti_3CN(OH)_x$@MoS_2 hybrids make their charge transfer fast and active sites exposure high, yielding a superior HER performance.

To fundamentally understand the excellent electrocatalytic activity of the quasi core–shell structural $Ti_3CN(OH)_x$@MoS_2 hybrids, theoretical calculations are performed based on a periodic DFT, and the resulting optimal atomic configurations are presented in Figs. 6(a) and 6(b), and Figs. S6 and S7 in the ESM. Generally, ΔG_H^* can well describe the activity of catalysts in acidic electrolytes, and the $|\Delta G_H^*|$ of the desired HER catalysts should be close to 0. Figure 6(c) summarizes the calculated ΔG_H^* for $Ti_3CN(OH)_x$, MoS_2, and $Ti_3CN(OH)_x$@MoS_2 hybrids. This figure reveals that the quasi core–shell structural $Ti_3CN(OH)_x$@MoS_2 hybrids have the smallest $|\Delta G_H^*|$, suggesting the presence of an accelerated rate-determining step of HER process by suitable adsorption characteristics originating from the electron transfer and charge distribution between $Ti_3CN(OH)_x$ and MoS_2.

4 Conclusions

In this work, *in situ* etching and hydrothermal processes are combined for a rational synthesis of the quasi core–shell structural carbonitride-based MXene $Ti_3CN(OH)_x$@MoS_2 hybrids. The as-prepared composite exhibits an enhanced electrical conductivity and a strong chemical coupling between the surface –OH groups of 2D carbonitride-based MXene Ti_3CNT_x nanosheets and the MoS_2 nanoflowers. Accordingly, the electrocatalyst delivers outstanding electrocatalytic HER performance in a 0.5 M H_2SO_4 electrolyte: an overpotential of 120 mV at a current density of 10 mA·cm^{-2}, a Tafel slope of 64 mV·dec^{-1}, and satisfactory long-term stability. Theoretical calculations reveal that the modulated electronic structure of the quasi core–shell structural $Ti_3CN(OH)_x$@MoS_2 hybrids endows the composite enhanced stability, excellent charge transfer kinetics, and optimal free adsorption energy of hydrogen, resulting in a remarkable HER performance. This work proposed a highly effective strategy for fabricating MXene-based hybrids for electrochemical energy storage and conversion.

Acknowledgements

This work was financially supported by the National Natural Science Foundation of China (Nos. 62004143 and 21902108), the Key Research and Development (R&D) Program of Hubei Province (No. 2022BAA084), the Central Government Guided Local Science and Technology Development Special Fund Project (No. 2020ZYYD033), the Natural Science Foundation of Hubei Province (No. 2021CFB133), and the Knowledge Innovation Program of Wuhan-Shuguang Project (No. 2022010801020355).

Electronic Supplementary Material: Supplementary material

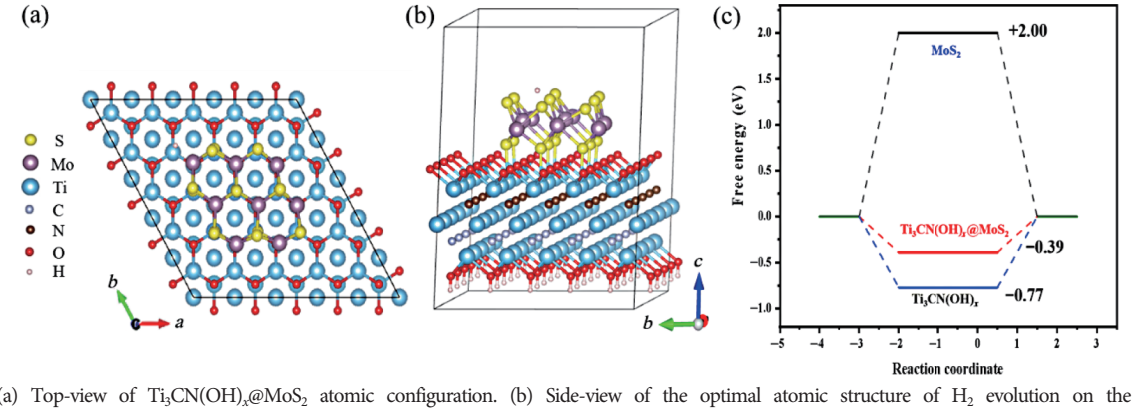

Figure 6 (a) Top-view of $Ti_3CN(OH)_x$@MoS_2 atomic configuration. (b) Side-view of the optimal atomic structure of H_2 evolution on the surface of $Ti_3CN(OH)_x$@MoS_2 hybrids. (c) ΔG_H diagrams of $Ti_3CN(OH)_x$, MoS_2, and $Ti_3CN(OH)_x$@MoS_2 hybrids.

(further details of theoretical calculations, side-view of three-dimensional (3D) CDD mapping of $Ti_3CN(OH)_x$@MoS_2, Raman spectra, HRTEM image, polarization curves at different hydrothermal times and temperatures, CV curves of different electrodes, and top and side views of the atomic structure of MoS_2 and $Ti_3CN(OH)_x$) is available in the online version of this article at https://doi.org/10.1007/s12274-022-5112-x.

References

[1] Zhu, P.; Xiong, X.; Wang, D. S. Regulations of active moiety in single atom catalysts for electrochemical hydrogen evolution reaction. *Nano Res.* **2022**, *15*, 5792–5815.

[2] Xiang, K.; Wu, D.; Deng, X. H.; Li, M.; Chen, S. Y.; Hao, P. P.; Guo, X. F.; Luo, J. L.; Fu, X. Z. Boosting H_2 generation coupled with selective oxidation of methanol into value-added chemical over cobalt hydroxide@hydroxysulfide nanosheets electrocatalysts. *Adv. Funct. Mater.* **2020**, *30*, 1909610.

[3] Yang, J. R.; Li, W. H.; Tan, S. D.; Xu, K. N.; Wang, Y.; Wang, D. S.; Li, Y. D. The electronic metal–support interaction directing the design of single atomic site catalysts: Achieving high efficiency towards hydrogen evolution. *Angew. Chem., Int. Ed.* **2021**, *60*, 19085–19091.

[4] Lei, Y. P.; Wang, Y. C.; Liu, Y.; Song, C. Y.; Li, Q.; Wang, D. S.; Li, Y. D. Designing atomic active centers for hydrogen evolution electrocatalysts. *Angew. Chem., Int. Ed.* **2020**, *59*, 20794–20812.

[5] Han, A. L.; Zhou, X. F.; Wang, X. J.; Liu, S.; Xiong, Q. H.; Zhang, Q. H.; Gu, L.; Zhuang, Z. C.; Zhang, W. J.; Li, F. X. et al. One-step synthesis of single-site vanadium substitution in 1T-WS_2 monolayers for enhanced hydrogen evolution catalysis. *Nat. Commun.* **2021**, *12*, 709.

[6] Jing, H. Y.; Zhu, P.; Zheng, X. B.; Zhang, Z. D.; Wang, D. S.; Li, Y. D. Theory-oriented screening and discovery of advanced energy transformation materials in electrocatalysis. *Adv. Powder Mater.* **2022**, *1*, 100013.

[7] Li, R. Z.; Wang, D. S. Understanding the structure–performance relationship of active sites at atomic scale. *Nano Res.* **2022**, *15*, 6888–6923.

[8] Jiang, J. Z.; Li, N.; Zou, J.; Zhou, X.; Eda, G.; Zhang, Q. F.; Zhang, H.; Li, L. J.; Zhai, T. Y.; Wee A. T. S. Synergistic additive-mediated CVD growth and chemical modification of 2D materials. *Chem. Soc. Rev.* **2019**, *48*, 4639–4654.

[9] Zou, J.; Wu, S. L.; Liu, Y.; Sun, Y. J.; Cao, Y.; Hsu, J. P.; Wee, A. T. S.; Jiang J. Z. An ultra-sensitive electrochemical sensor based on 2D g-C_3N_4/CuO nanocomposites for dopamine detection. *Carbon* **2018**, *130*, 652–663.

[10] Jiang, J. Z.; Ouyang, L.; Zhu, L. H.; Zheng, A. M.; Zou, J.; Yi, X. F.; Tang, H. Q. Dependence of electronic structure of g-C_3N_4 on the layer number of its nanosheets: A study by Raman spectroscopy coupled with first-principles calculations. *Carbon* **2014**, *80*, 213–221.

[11] Bai, S. S.; Yang, M. Q.; Jiang, J. Z.; He, X. M.; Zou, J.; Xiong, Z. G.; Liao, G. D.; Liu, S. Recent advances of MXenes as electrocatalysts for hydrogen evolution reaction. *npj 2D Mater. Appl.* **2021**, *5*, 78.

[12] Zou, J.; Wu, J.; Wang, Y. Z.; Deng, F. X.; Jiang, J. Z.; Zhang, Y. Z.; Liu, S.; Li, N.; Zhang, H.; Yu, J. G. et al. Additive-mediated intercalation and surface modification of MXenes. *Chem. Soc. Rev.* **2022**, *51*, 2972–2990.

[13] Jiang, J. Z.; Zou, Y. L.; Arramel, Li, F. Y.; Wang, J. M.; Zou, J.; Li, N. Intercalation engineering of MXenes towards highly efficient photo(electrocatalytic) hydrogen evolution reactions. *J. Mater. Chem. A* **2021**, *9*, 24195–24214.

[14] Zeng, Z. L.; Chen, X. Z.; Weng, K. Y.; Wu, Y.; Zhang, P.; Jiang, J. Z.; Li, N. Computational screening study of double transition metal carbonitrides M'$_2$M"CNO_2-MXene as catalysts for hydrogen evolution reaction. *npj Comput. Mater.* **2021**, *7*, 80.

[15] Ding, B.; Ong, W. J.; Jiang, J. Z.; Chen, X. Z.; Li, N. Uncovering the electrochemical mechanisms for hydrogen evolution reaction of heteroatom doped M_2C MXene (M = Ti, Mo). *Appl. Surf. Sci.* **2020**, *500*, 143987.

[16] Jiang, J. Z.; Bai, S. S.; Zou, J.; Liu, S.; Hsu, J. P.; Li, N.; Zhu, G. Y.; Zhuang, Z. C.; Kang, Q.; Zhang, Y. Z. Improving stability of MXenes. *Nano Res.* **2022**, *15*, 6551–6567.

[17] Li, N.; Peng, J. H.; Ong, W. J.; Ma, T. T.; Arramel, Zhang, P.; Jiang, J. Z.; Yuan, X. F.; Zhang, C. F. MXenes: An emerging platform for wearable electronics and looking beyond. *Matter* **2021**, *4*, 377–407.

[18] Jiang, J. Z.; Bai, S. S.; Yang, M. Q.; Zou, J.; Li, N.; Peng, J. H.; Wang, H. T.; Xiang, K.; Liu, S.; Zhai, T. Y. Strategic design and fabrication of MXenes-Ti_3CNCl_2@CoS_2 core–shell nanostructure for high-efficiency hydrogen evolution. *Nano Res.* **2022**, *15*, 5977–5986.

[19] Jiang, Y. N.; Sun, T.; Xie, X.; Jiang, W.; Li, J.; Tian, B. B.; Su, C. L. Oxygen-functionalized ultrathin $Ti_3C_2T_x$ MXene for enhanced electrocatalytic hydrogen evolution. *ChemSusChem* **2019**, *12*, 1368–1373.

[20] Lim, K. R. G.; Handoko, A. D.; Johnson, L. R.; Meng, X.; Lin, M.; Subramanian, G. S.; Anasori, B.; Gogotsi, Y.; Vojvodic, A.; Seh, Z. W. 2H-MoS_2 on Mo_2CT_x MXene nanohybrid for efficient and durable electrocatalytic hydrogen evolution. *ACS Nano* **2020**, *14*, 16140–16155.

[21] Du, C. F.; Dinh, K. N.; Liang, Q. H.; Zheng, Y.; Luo, Y. B.; Zhang, J. L.; Yan, Q. Y. Self-assemble and *in situ* formation of $Ni_{1-x}Fe_xPS_3$ nanomosaic-decorated MXene hybrids for overall water splitting. *Adv. Energy Mater.* **2018**, *8*, 1801127.

[22] Wang, H.; Lee, J. M. Recent advances in structural engineering of MXene electrocatalysts. *J. Mater. Chem. A* **2020**, *8*, 10604–10624.

[23] Wang, J. Y.; He, P. L.; Shen, Y. L.; Dai, L. X.; Li, Z.; Wu, Y.; An, C. H. FeNi nanoparticles on $Mo_2TiC_2T_x$ MXene@nickel foam as robust electrocatalysts for overall water splitting. *Nano Res.* **2021**, *14*, 3474–3481.

[24] Yan, L.; Zhang, B. Rose-like, ruthenium-modified cobalt nitride nanoflowers grown *in situ* on an MXene matrix for efficient and stable water electrolysis. *J. Mater. Chem. A* **2021**, *9*, 20758–20765.

[25] Li, S. X.; Que, X. Y.; Chen, X. B.; Lin, T. R.; Sheng, L.; Peng, J.; Li, J. Q.; Zhai, M. L. One-step synthesis of modified Ti_3C_2 MXene-supported amorphous molybdenum sulfide electrocatalysts by a facile gamma radiation strategy for efficient hydrogen evolution reaction. *ACS Appl. Energy Mater.* **2020**, *3*, 10882–10891.

[26] Kuang, P. Y.; He, M.; Zhu, B. C.; Yu, J. G.; Fan, K.; Jaroniec, M. 0D/2D NiS_2/V-MXene composite for electrocatalytic H_2 evolution. *J. Catal.* **2019**, *375*, 8–20.

[27] Yan, L.; Zhang, B.; Wu, S. Y.; Yu, J. L. A general approach to the synthesis of transition metal phosphide nanoarrays on MXene nanosheets for pH-universal hydrogen evolution and alkaline overall water splitting. *J. Mater. Chem. A* **2020**, *8*, 14234–14242.

[28] Zong, H.; Qi, R. J.; Yu, K.; Zhu, Z. Q. Ultrathin Ti_2NT_x MXene-wrapped MOF-derived CoP frameworks towards hydrogen evolution and water oxidation. *Electrochim. Acta* **2021**, *393*, 139068.

[29] Wang, H.; Lin, Y. P.; Liu, S. Y.; Li, J. M.; Bu, L. M.; Chen, J. M.; Xiao, X.; Choi, J. H.; Gao, L. J.; Lee, J. M. Confined growth of pyridinic N-Mo_2C sites on MXenes for hydrogen evolution. *J. Mater. Chem. A* **2020**, *8*, 7109–7116.

[30] Shen, B. F.; Huang, H. J.; Jiang, Y.; Xue, Y.; He, H. Y. 3D interweaving MXene-graphene network-confined Ni-Fe layered double hydroxide nanosheets for enhanced hydrogen evolution. *Electrochim. Acta* **2022**, *407*, 139913.

[31] Deng, L. Q.; Chang, B.; Shi, D.; Yao, X. G.; Shao, Y. L.; Shen, J. X.; Zhang, B. G.; Wu, Y. Z.; Hao, X. P. MXene decorated by phosphorus-doped TiO_2 for photo-enhanced electrocatalytic hydrogen evolution reaction. *Renew. Energy* **2021**, *170*, 858–865.

[32] Shinde, P. V.; Mane, P.; Chakraborty, B.; Rout, C. S. Spinel $NiFe_2O_4$ nanoparticles decorated 2D Ti_3C_2 MXene sheets for efficient water splitting: Experiments and theories. *J. Colloid Interface Sci.* **2021**, *602*, 232–241.

[33] Liu, D.; Lv, Z. P.; Dang, J.; Ma, W. S.; Jian, K. L.; Wang, M.; Huang, D. J.; Tian, W. Q. Nitrogen-doped MoS_2/$Ti_3C_2T_x$ heterostructures as ultra-efficient alkaline HER electrocatalysts. *Inorg. Chem.* **2021**, *60*, 9932–9940.

[34] Huang, H. J.; Xue, Y.; Xie, Y. S.; Yang, Y.; Yang, L.; He, H. Y.; Jiang, Q. G.; Ying, G. B. MoS_2 quantum dot-decorated MXene nanosheets as efficient hydrogen evolution electrocatalysts. *Inorg. Chem. Front.* **2022**, *9*, 1171–1178.

[35] Lin, H.; Chen, L. S.; Lu, X. Y.; Yao, H. L.; Chen, Y.; Shi, J. L. Two-dimensional titanium carbide MXenes as efficient non-noble metal electrocatalysts for oxygen reduction reaction. *Sci. China Mater.* **2019**, *62*, 662–670.

[36] Zheng, X.; Wang, Z. L.; Li, J. J.; Wei, L. M. Binder-free S@$Ti_3C_2T_x$ sandwich structure film as a high-capacity cathode for a stable aluminum-sulfur battery. *Sci. China Mater.* **2022**, *65*, 1463–1475.

[37] Xu, H. Y.; Zheng, R. X.; Du, D. Y.; Ren, L. F.; Li, R. J.; Wen, X. J.; Zhao, C.; Zeng, T.; Zhou, B.; Shu, C. Z. Cationic vanadium vacancy-enriched $V_{2-x}O_5$ on V_2C MXene as superior bifunctional electrocatalysts for Li-O_2 batteries. *Sci. China Mater.* **2022**, *65*, 1761–1770.

[38] He, F. Y.; Tang, C.; Zhu, G. J.; Liu, Y. D.; Du, A. J.; Zhang, Q. B.; Wu, M. H.; Zhang, H. J. Leaf-inspired design of mesoporous Sb_2S_3/N-doped $Ti_3C_2T_x$ composite towards fast sodium storage. *Sci. China Chem.* **2021**, *64*, 964–973.

[39] Cao, P. F.; Peng, J.; Li, J. Q.; Zhai, M. L. Highly conductive carbon black supported amorphous molybdenum disulfide for efficient hydrogen evolution reaction. *J. Power Sources* **2017**, *347*, 210–219.

[40] Xie, J. F.; Zhang, H.; Li, S.; Wang, R. X.; Sun, X.; Zhou, M.; Zhou, J. F.; Lou, X. W.; Xie, Y. Defect-rich MoS_2 ultrathin nanosheets with additional active edge sites for enhanced electrocatalytic hydrogen evolution. *Adv. Mater.* **2013**, *25*, 5807–5813.

[41] Wang, X.; Li, H.; Li, H.; Lin, S.; Ding, W.; Zhu, X. G.; Sheng, Z. G.; Wang, H.; Zhu, X. B.; Sun, Y. P. 2D/2D 1T-MoS_2/Ti_3C_2 MXene heterostructure with excellent supercapacitor performance. *Adv. Funct. Mater.* **2020**, *30*, 0190302.

[42] Zhang, J. P.; Li, Y. X.; Xu, C. Y.; Li, J.; Yang, L. Y.; Yin, S. G. 2D/2D/1D structure of a self-supporting electrocatalyst for efficient hydrogen evolution. *ACS Appl. Energy Mater.* **2022**, *5*, 1710–1719.

[43] Wang, H. Q.; Wang, J. W.; Wang, X. Z.; Gao, X. H.; Zhuang, G. C.; Yang, J. B.; Ren, H. Dielectric properties and energy storage performance of PVDF-based composites with MoS_2@MXene nanofiller. *Chem. Eng. J.* **2022**, *437*, 135431.

[44] Bai, J.; Zhao, B. C.; Lin, S.; Li, K. Z.; Zhou, J. F.; Dai, J. M.; Zhu, X. B.; Sun, Y. P. Construction of hierarchical V_4C_3-MXene/MoS_2/C nanohybrids for high rate lithium-ion batteries. *Nanoscale* **2020**, *12*, 1144–1154.

[45] Zhang, Y.; Huang, Y.; Zhu, S. S.; Liu, Y. Y.; Zhang, X.; Wang, J. J.; Braun, A. Covalent S–O bonding enables enhanced photoelectrochemical performance of Cu_2S/Fe_2O_3 heterojunction for water splitting. *Small* **2021**, *17*, 2100320.

[46] Ramalingam, V.; Varadhan, P.; Fu, H. C.; Kim, H.; Zhang, D. L.; Chen, S. M.; Song, L.; Ma, D.; Wang, Y.; Alshareef, H. N. et al. Heteroatom-mediated interactions between ruthenium single atoms and an MXene support for efficient hydrogen evolution. *Adv. Mater.*, **2019**, *31*, 1903841.

[47] Wang, Y.; Zheng, X. B.; Wang, D. S. Design concept for electrocatalysts. *Nano Res.* **2022**, *15*, 1730–1752.